applied sciences

MDPI

Article

Force Analysis of Circular Diaphragm Wall Based on Circular Cylindrical Shell Theory

Lin Wang [1,2,*] and Guojian Shao [1]

[1] College of Mechanics and Materials, Hohai University, Nanjing 211100, China; gjshao@hhu.edu.cn
[2] School of Civil Engineering, Jiangsu College of Engineering and Technology, Nantong 226007, China
* Correspondence: wanglinhs@126.com

Abstract: In order to make up for the shortcomings of existing theory calculation methods for circular diaphragm walls, an alternative calculation method was developed with a clear concept based on the circular cylindrical shell theory and superposition principle in elasticity and named the circular cylindrical shell theory calculation method (CCSTCM). We took the north anchorage circular foundation pit of G3 Tongling Yangtze River Highway and Railway Bridge as an example and calculated and analyzed it by the proposed CCSTCM, finite element numerical simulation method (FENSM) and site monitoring. As a result, we obtained the radial displacement, circumferential stress and vertical bending moment of the circular diaphragm wall, and then summarized their regularities. By researching the results of the CCSTCM (TCR), the results of the FENSM (NSR) and the results of the site monitoring (SMR), the following conclusions could be drawn: the numerical calculation model established was reasonable; the variation trends of the data curves of the TCR were highly similar to those of the NSR and SMR; and the TCR were slightly larger than the NSR but slightly smaller than the SMR, and closer to the SMR in general. Finally, the proposed CCSTCM was proven to be correct and applicable and could be used in similar circular diaphragm wall projects.

Keywords: circular cylindrical shell theory; circular diaphragm wall; radial displacement; circumferential stress; vertical bending moment

check for updates

Citation: Wang, L.; Shao, G. Force Analysis of Circular Diaphragm Wall Based on Circular Cylindrical Shell Theory. *Appl. Sci.* **2023**, *13*, 4450. https://doi.org/10.3390/app13074450

Academic Editors: Ichiro Ario, Yuki Chikahiro and Gakuho Watanabe

Received: 3 February 2023
Revised: 22 March 2023
Accepted: 28 March 2023
Published: 31 March 2023

Copyright: © 2023 by the authors. Licensee MDPI, Basel, Switzerland. This article is an open access article distributed under the terms and conditions of the Creative Commons Attribution (CC BY) license (https://creativecommons.org/licenses/by/4.0/).

1. Introduction

As the diaphragm wall has the three functions of retaining soil, bearing load and proofing water, it has become one of the most widely used support forms in foundation pit engineering. In particular, the circular diaphragm wall has been widely used in deep and large foundation pits in urban areas and for large bridge anchorages as its circular arch effect can produce less deformation, smaller internal force and higher stability [1–5]. Therefore, many scholars and engineering practitioners have carried out a series of researches on circular diaphragm walls, especially on the deformation and internal force of the wall body. They mainly use three research methods: the theoretical calculation method of physics and mechanics, the numerical simulation method, and the site monitoring method.

In the theoretical calculation method, the Chinese specification [6] recommends adopting the beam-on-elastic-foundation method, which is also described in the literature [7] and used widely for its simple model, clear concept, and consideration of the arch effect of circular diaphragm walls. However, the circumferential force of circular diaphragm walls and reinforced concrete lining (hereinafter referred to as lining) cannot be calculated by this method, and the calculation results are often conservative. There are a number of calculation methods for linear diaphragm walls, and a smaller amount for circular diaphragm walls, and most of the empirical or semi-empirical methods are derived from linear diaphragm walls [8–15]. Comparatively speaking, there are few theoretical calculation methods for the deformation and internal force of circular diaphragm walls. Liu et al. [16] analyzed the internal force and displacement in walls with different thicknesses, radiuses and

depths based on the analytical solution of internal force and displacement of circular diaphragm walls, and they discussed the pattern of the internal force, which changed with the body characteristics. Cui et al. [17] established a functional to solve the displacement of the circular diaphragm wall based on the basic three-dimensional elasticity equations of cylindrical shells under the action of axial symmetric loads. They obtained the solution equations of the displacement function with the variational principle by introducing a single Fourier series as the trial function of displacement and put forward the Ritz method of the circular diaphragm wall after finally combining it with the boundary conditions.

Some scholars use the numerical simulation method to research the mechanical response of only the circular foundation pit (e.g., Cai et al., 2002; Arai et al., 2008; Borges and Guerra, 2014; Wu et al., 2017) [18–21]. Some scholars adopt the site monitoring method to study the mechanical response of circular foundation pits and compare the field monitoring data with the existing research results or the theoretical calculation results, so as to provide reference experience and methods for the design and construction of circular ground walls (e.g., Tan and Wang, 2013; Tan and Wang, 2015; Kumagai et al., 1999; Parashar et al., 2007; Jia et al., 2019) [1,7,22–24]. Some scholars utilize the site monitoring method and numerical simulation method at the same time to study the mechanical response of circular foundation pits, in order to compare and analyze the results from the two methods and make the conclusion more convincing (e.g., Gao et al., 2023; Cabarkapa et al., 2010; Schwamb, 2014; Schwamb et al., 2015; Shi et al. 2022) [5,25–28]. However, it is difficult to set the material parameters of the model and the contacts between different parts accurately when the numerical simulation method is utilized, and the calculation cost is also very large. The parameters in the numerical calculation model are different for different construction sites, and therefore the parameters chosen should not be identical. The calculation process may not converge for these complex models. The site monitoring method has a hysteresis quality and the monitoring instruments and process are easily interfered with by external factors, such as temperature and mechanical load, which leads to some errors in the monitoring data obtained.

In view of the shortcomings of existing research methods for the deformation and internal force of circular diaphragm walls, according to its own structural characteristics and mechanical characteristics, the alternative calculation method with a clear concept will be developed based on the circular cylindrical shell theory and superposition principle in elasticity, and the specific analytical solutions will be given. This method will be named the circular cylindrical shell theory calculation method (CCSTCM). Taking the north anchorage circular foundation pit of G3 Tongling Yangtze River Highway and Railway Bridge in Anhui Province China as a case study, the proposed CCSTCM will be adopted to perform a calculation; the numerical model of the case will be built and the finite element numerical simulation method (FENSM) will be used to calculate; and site monitoring will also be carried out. Then, the results of the CCSTCM (hereinafter referred to as TCR) and results of FENSM (hereinafter referred to as NSR) will be compared with the measured results from the site monitoring (hereinafter referred to as SMR), the regularity of the results will be summarized and researched, and the correctness and applicability of the numerical model and the proposed CCSTCM will be verified. In this way, the safety and stability of the north anchorage foundation pit will be evaluated and the reinforcement measures and matters needing attention will be proposed in the construction process, based on the results. This research will provide a reference for the design and construction of other similar circular diaphragm wall projects.

2. Project Profile

The G3 Tongling Yangtze River Highway and Railway Bridge is a project under construction instead of the existing Tongling Yangtze River Highway Bridge, which connects the downtown area of Tongling on the south bank of the Yangtze River with the suburban area and the Zongyang County of Tongling on the north bank of the Yangtze River. The bridge is constructed according to the standard of “4-line railway + 6-lane

expressway". The four-line railway include two lines of prepared intercity railways and two lines of universal speed railways, from the south of Tongling to the Port in the north of the Yangtze River. The six-lane expressway is the six-lane G3 Beijing-Taipei Expressway with emergency parking belts on both sides. Combined, the railway and expressway of the bridge is 2682.2 m long. The main bridge is 1505 m long, and the main span is 988 m long. The approach bridge—the combination of the railway and expressway on the north of the Yangtze River—is 686.7 m long, and the approach bridge combining the railway and expressway on the south of the Yangtze River is 490.5 m long. The bridge adopts the joint type of cable-stayed bridge and suspension bridge and is designed as a cable-stayed suspension composite bridge. The north anchorage on the Zongyang Bank and the south anchorage on the Tongling Bank are the main components that bear the oblique tension. In this study, only the force and deformation of the circular diaphragm wall of the north anchorage foundation pit will be discussed in the construction process.

The design size of the north anchorage is shown in Figures 1 and 2. The diaphragm wall of the foundation pit is a circular structure that is 1.5 m thick, and its outer diameter is 60 m long. Its bottom elevation is −50.500 m, its top elevation is +5.000 m, and its height is 55.5 m (excluding the cap beam). The circular diaphragm wall is divided into 40 slots, and there are 20 slots in the first-stage project, with a center-line arc length of 6.885 m, and 20 slots in the second-stage project, with a center-line arc length of 2.8 m. The cap beam is connected with the top of the circular diaphragm wall, with a total width of 4.5 m and a total height of 2 m, and the boundaries of the cap beam exceed both the inner and outer sides of circular diaphragm wall by 1.5 m. The excavation depth of the foundation pit is 47 m from the top of the cap beam to the bottom of the foundation. In order to meet the safety requirements of the circular diaphragm wall during the excavation stage of the foundation pit, the lining is set on the inner side of the circular diaphragm wall with a total height of 45 m. The thickness of the upper part (from 0 m to 15 m) of the lining is 1.5 m, that of the middle part (from 15 m to 30 m) is 2.0 m, and that of the lower part (from 30 m to 45 m) is 2.5 m. The circular diaphragm wall, cap beam and lining are all made of the same reinforced concrete. The strength grade of the concrete is C35 and it has an elastic modulus of 31.5 GPa, a Poisson's ratio of 0.2 and a bulk density of 25 kN/m^3. The foundation pit was excavated in layers using a top-down method, and one layer of lining (each layer is 3 m in height) was constructed after one layer of soil had been excavated, with a total of 15 layers. The specific construction situation is shown in Figure 2 and Table 1.

Table 1. Construction situation of the north anchorage foundation pit.

Working Condition	Construction Content	Start Date	Finish Date	Thickness/m
0-1	Constructed the circular diaphragm wall, excavated the overlying soil layer, and chiseled away the slurry at the top of circular diaphragm wall	27 June 2022	24 July 2022	4.14
0-2	Excavated the cap beam layer of soil	25 July 2022	30 July 2022	2
	Constructed the cap beam layer of reinforced concrete	27 July 2022	13 August 2022	3
W1	Excavated the 1st layer of soil	10 August 2022	21 August 2022	3
	Constructed the 1st lining layer of reinforced concrete	16 August 2022	25 August 2022	3
W2	Excavated the 2nd layer of soil	23 August 2022	30 August 2022	3
	Constructed the 2nd lining layer of reinforced concrete	26 August 2022	5 September 2022	3
W3	Excavated the 3rd layer of soil	31 August 2022	6 September 2022	3
	Constructed the 3rd lining layer of reinforced concrete	6 September 2022	12 September 2022	3
W4	Excavated the 4th layer of soil	7 September 2022	13 September 2022	3
	Constructed the 4th lining layer of reinforced concrete	13 September 2022	17 September 2022	3

Table 1. *Cont.*

Working Condition	Construction Content	Start Date	Finish Date	Thickness/m
W5	Excavated the 5th layer of soil	14 September 2022	19 September 2022	3
	Constructed the 5th lining layer of reinforced concrete	18 September 2022	23 September 2022	3
W6	Excavated the 6th layer of soil	20 September 2022	26 September 2022	3
	Constructed the 6th lining layer of reinforced concrete	24 September 2022	29 September 2022	3
W7	Excavated the 7th layer of soil	27 September 2022	4 October 2022	3
	Constructed the 7th lining layer of reinforced concrete	30 September 2022	6 October 2022	3
W8	Excavated the 8th layer of soil	5 October 2022	10 October 2022	3
	Constructed the 8th lining layer of reinforced concrete	7 October 2022	12 October 2022	3
W9	Excavated the 9th layer of soil	11 October 2022	15 October 2022	3
	Constructed the 9th lining layer of reinforced concrete	13 October 2022	18 October 2022	3
W10	Excavated the 10th layer of soil	16 October 2022	22 October 2022	3
	Constructed the 10th lining layer of reinforced concrete	19 October 2022	25 October 2022	3
W11	Excavated the 11th layer of soil	23 October 2022	28 October 2022	3
	Constructed the 11th lining layer of reinforced concrete	26 October 2022	1 November 2022	3
W12	Excavated the 12th layer of soil	29 October 2022	5 November 2022	3
	Constructed the 12th lining layer of reinforced concrete	2 November 2022	8 November 2022	3
W13	Excavated the 13th layer of soil	6 November 2022	11 November 2022	3
	Constructed the 13th lining layer of reinforced concrete	9 November 2022	17 November 2022	3
W14	Excavated the 14th layer of soil	12 November 2022	25 November 2022	3
	Constructed the 14th lining layer of reinforced concrete	18 November 2022	28 November 2022	3
W15	Excavated the 15th layer of soil	26 November 2022	5 December 2022	3
	Constructed the 15th lining layer of reinforced concrete	29 November 2022	30 December 2022	3

The north anchorage is located on the first terrace of the north bank of the Yangtze River, about 60 m away from the Yangtze River levee. The site where the north anchorage is located has a flat terrain, little fluctuation in bedrock, and a thick overburden range of 45.0 m to 47.0 m. The specific distribution and physical and mechanical parameters of the surrounding soil layers are shown in Figure 1 and Table 2. When the CCSTCM or FENSM are adopted, the uniform distribution normal pressure applied on the upper surface of the surrounding soil layer is considered to be q_0 = 80 kPa.

Table 2. Physical and mechanical parameters of the soil around the circular diaphragm wall.

Code	Classification	Thickness/m	Bulk Density/ (kN/m^3)	Young's Modulus/MPa	Poisson's Ratio	Cohesion/kPa	Internal Friction Angle/°
①	Silty clay	1.26	18.62	129	0.3	21.5	11.3
②	MSC	7.6	17.64	93	0.3	10.3	6.6
③	Silt	16	18.5	305	0.3	10	20
④	Fine sand	14	19	341	0.3	0	24
⑤	FBS	2	22	975	0.3	0	45
⑥	HWAS	3	22.83	1227	0.2	150	25
⑦	WCC	2.1	23.03	4117	0.2	200	40
⑧	MCAS	11.54	23.42	4408	0.2	200	30

Note: MSC represents the mucky silty clay; FBS represents the fine boulder soil; HWAS represents the highly weathered argillaceous sandstone; WCC represents the weakly consolidated conglomerate; MCAS represents the moderately consolidated argillaceous sandstone.

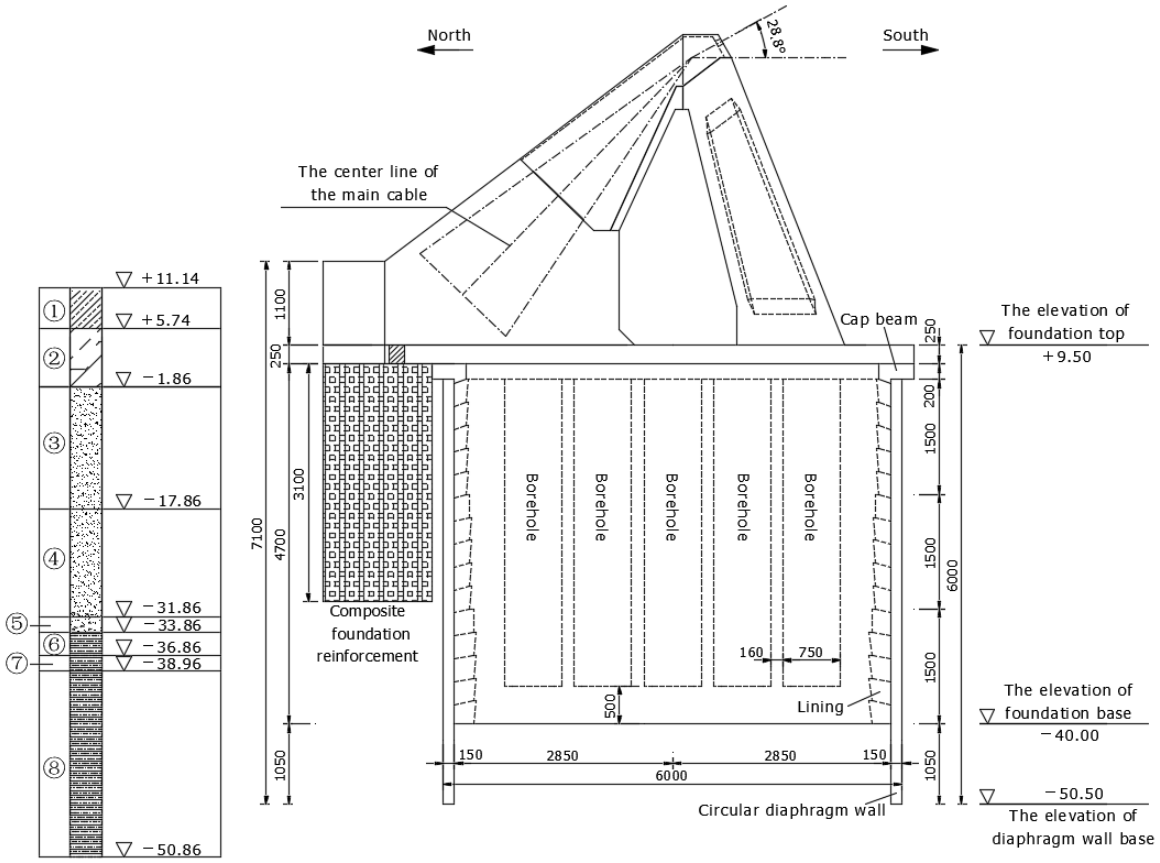


Figure 1. Design size of the north anchorage (the unit of elevation is "m", and the rest are in "cm").

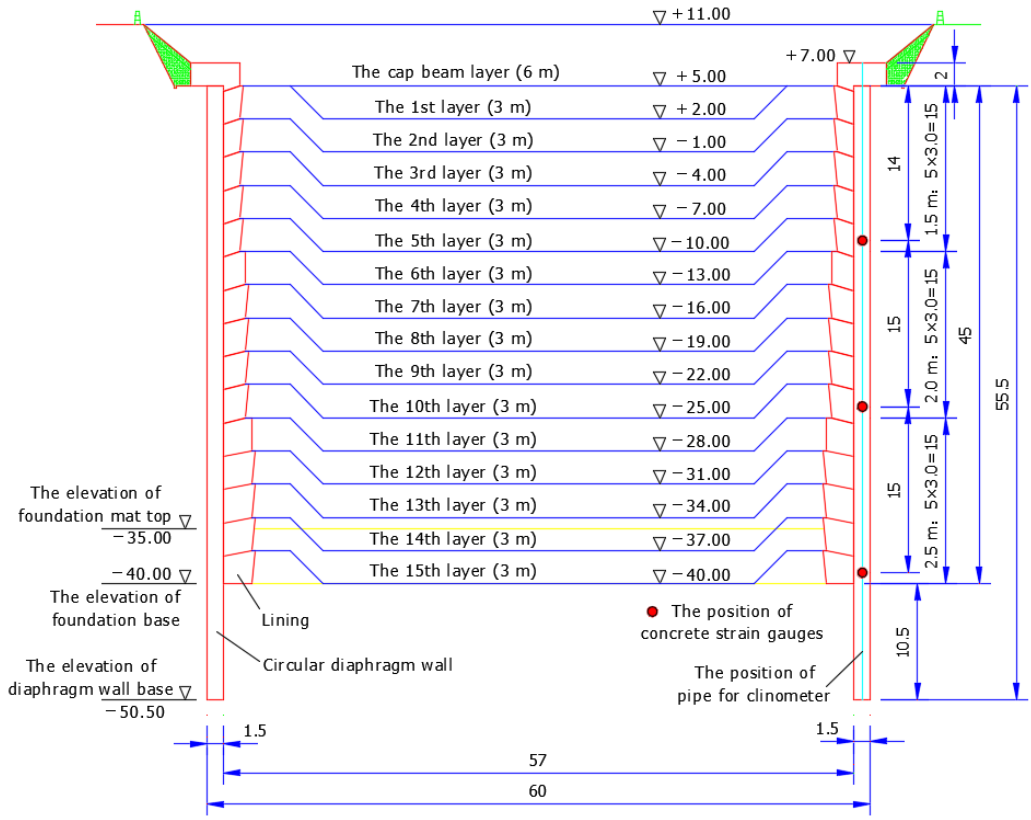
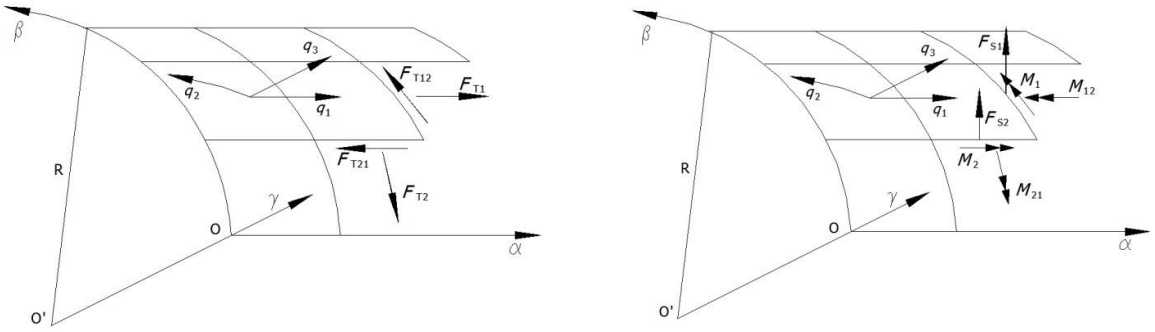


Figure 2. Layered excavation schematic diagram of the foundation pit (the unit is "m").

3. Force Analysis of Circular Diaphragm Wall

A body defined by two surfaces is called a shell if the distance between the surfaces is much smaller than the other dimensions of the body. The face formed by the points that are equidistant from the two surfaces is called the middle face. The shell with the cylindrical face as the middle face is called the cylindrical shell. Furthermore, if the middle face of the cylindrical shell is a circular cylindrical face, this is called the circular cylindrical shell [29]. As shown in Figure 3, in the engineering case, the thickness δ of the circular diaphragm wall is 1.5 m, the radius R of the middle face of the circular diaphragm wall is 28.5 m, and the ratio of δ to R approaches 1/20; hence, this can be simplified into a circular cylindrical shell for force analysis [30]. According to the literature [29], for thin circular cylindrical shells, a curvilinear coordinate system can be selected for mechanical calculation. Coordinate α is placed in the longitudinal direction, which is the direction of the generatrix of the middle face. Coordinate β is placed in the circumferential direction, which is the direction of the directrix of the middle face. Coordinate γ is placed in the radial direction, which is the direction of the thickness of the middle face. As shown in Figure 4, the circular diaphragm wall is mainly subjected to four kinds of horizontal external forces, including the horizontal supporting force of the cap beam, the horizontal supporting force of the lining, the horizontal subgrade reaction on the pit-facing surface of the circular diaphragm wall, and the horizontal earth pressure on the pit-back surface of the circular diaphragm wall.



(**a**) (**b**)

Figure 3. Curvilinear coordinate system for the cylindrical shell and internal forces. (**a**) Membrane internal forces. (**b**) Bending internal forces.

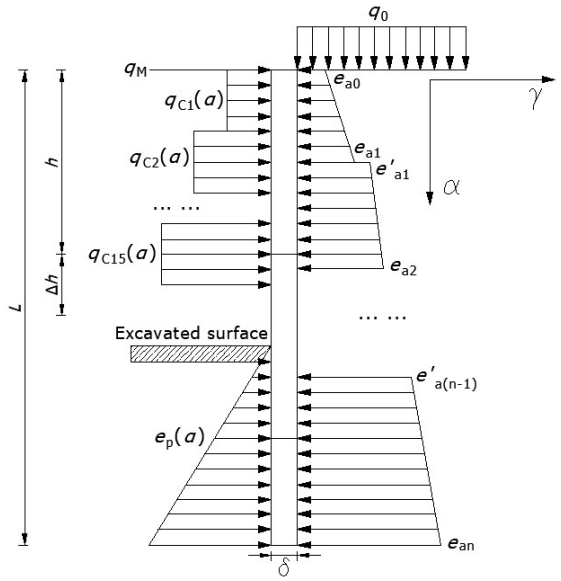


Figure 4. Circular diaphragm wall model under normal loads.

3.1. Horizontal Supporting Force of the Cap Beam

The cap beam has the effect of horizontal support at the top of the circular diaphragm wall, which is considered to be the normal uniform distribution force q_M along the circumference of the top surface of the circular diaphragm wall, as shown in Figure 4. q_M can be calculated by using Equation (1) below. In Equation (1), K_M represents the supporting stiffness of the cap beam; $w(0)$ represents the horizontal displacement at the top ($\alpha = 0$) of the circular diaphragm wall, caused by the excavation of the soil layer with Δh in thickness in every condition; E_M represents the Young's modulus of the cap beam material; A_M represents the effective section area of the cap beam; and R_M represents the central radius of the cap beam.

$$q_M = K_M \cdot w(0) = \frac{E_M A_M}{R_M^2} \cdot w(0) \tag{1}$$

3.2. Horizontal Supporting Force of the Lining

As shown in Figure 4, the horizontal support effects of the linings are considered as the distributed forces q_{Ci}, which are exerted on the pit-facing surface of the circular diaphragm wall at the corresponding position in the normal direction. Along direction α, the normal distributed forces q_{Ci} per unit depth can be expressed by Equation (2) below. In Equation (2), K_{Ci} represents the support stiffness per unit depth of the lining at Layer i; i represents the lining layers or the soil layers from the 1st layer to the 15th layer, and the values are 1, 2, 3, ... 15; $w(\alpha)$ represents the horizontal displacement at a depth of α, caused by the excavation of the soil layer with Δh in thickness in every working condition; E_C represents the Young's modulus of the lining material; δ_{Ci} represents the thickness of the lining at Layer i; and R_{Ci} represents the central radius of the lining at Layer i.

$$q_{Ci}(\alpha) = K_{Ci} \cdot w(\alpha) = \frac{E_C \delta_{Ci}}{R_{Ci}^2} \cdot w(\alpha) \tag{2}$$

3.3. Horizontal Subgrade Reaction on the Pit-Facing Surface

As shown in Figure 4, the horizontal subgrade reaction $e_p(\alpha)$ on the pit-facing surface of the circular diaphragm wall could be calculated with the "m" method provided in the literature [6], thus $e_p(\alpha)$ can be expressed by the following Equation (3). In Equation (3), m represents the horizontal subgrade reaction coefficient; h represents the excavation depth of the foundation pit before the Δh is excavated; and $w(\alpha)$ represents the same mean as before.

$$e_p(\alpha) = m(\alpha - h - \Delta h)w(\alpha) \tag{3}$$

3.4. Horizontal Earth Pressure on the Pit-Back Surface

As shown in Table 2 and Figure 4, the horizontal earth pressure e_{an} and e'_{an} on the pit-back surface of the circular diaphragm wall could be calculated through the Rankine active earth pressure theory by considering earth and water pressure together. The Rankine active earth pressure calculation process for cohesive soil is shown as follows.

The earth pressure strength of Layer ① can be obtained by Equations (4) and (5).

$$e_{a0} = q_0 \tan^2\left(45^\circ - \frac{\phi_1}{2}\right) - 2c_1 \tan\left(45^\circ - \frac{\phi_1}{2}\right) \tag{4}$$

$$e_{a1} = (q_0 + \gamma_1 \alpha_1) \tan^2\left(45^\circ - \frac{\phi_1}{2}\right) - 2c_1 \tan\left(45^\circ - \frac{\phi_1}{2}\right) \tag{5}$$

The earth pressure strength of Layer ② can be obtained by Equations (6) and (7).

$$e'_{a1} = (q_0 + \gamma_1 \alpha_1) \tan^2\left(45^\circ - \frac{\phi_2}{2}\right) - 2c_2 \tan\left(45^\circ - \frac{\phi_2}{2}\right) \tag{6}$$

$$e_{a2} = (q_0 + \gamma_1\alpha_1 + \gamma_2\alpha_2)\tan^2\left(45^\circ - \frac{\phi_2}{2}\right) - 2c_2\tan\left(45^\circ - \frac{\phi_2}{2}\right) \quad (7)$$

. . . . . .

The earth pressure strength of Layer n can be obtained by Equations (8) and (9).

$$e'_{a(n-1)} = (q_0 + \gamma_1\alpha_1 + \gamma_2\alpha_2 + \ldots + \gamma_{n-1}\alpha_{n-1})\tan^2\left(45^\circ - \frac{\phi_n}{2}\right) - 2c_n\tan\left(45^\circ - \frac{\phi_n}{2}\right) \quad (8)$$

$$e_{an} = (q_0 + \gamma_1\alpha_1 + \gamma_2\alpha_2 + \ldots + \gamma_n\alpha_n)\tan^2\left(45^\circ - \frac{\phi_n}{2}\right) - 2c_n\tan\left(45^\circ - \frac{\phi_n}{2}\right) \quad (9)$$

In Equation (9), q_0 represents the applied load above the calculation surface; γ_n represents the bulk density of the rock or soil at Layer n; φ_n represents the internal friction angle of the rock or soil at Layer n; and c_n represents the cohesion of the rock or soil at Layer n. For in cohesive soil, the cohesion c_n is just set to 0.

4. Circular Cylindrical Shell Theory Calculation Method (CCSTCM)

4.1. Internal Force Expressions of Cylindrical Shell

The cylindrical shell is a special case of the shell in elasticity, and the equilibrium differential equations of the cylindrical shell can be expressed by Equation (10) under arbitrary load [29]. In Equation (10), as shown in Figure 3, F_{T1} represents the tension or pressure applied on the unit width of the middle face on face α; F_{T12} represents the leveling force applied on the unit width of the middle surface on Surface α; F_{T2} represents the tension or pressure applied on the unit width of the middle face on face β; F_{T21} represents the leveling force applied on the unit width of the middle face on face β, and F_{T21}=F_{T12}. These four internal forces are called membrane internal forces. M_1 represents the bending moment applied on the unit width of the middle face on face α; M_{12} represents the torque applied on the unit width of the middle face on face α; F_{S1} represents the transverse shear force applied on the unit width of the middle face on face α; M_2 represents the bending moment applied on the unit width of the middle face on face β; M_{21} represents the torque applied on the unit width of the middle face on face β, and M_{21}=M_{12}; and F_{S2} represents the transverse shear force applied on the unit width of the middle face on face β. These six internal forces are called bending internal forces. q_1, q_2 and q_3 represent the distribution loads applied on the cylindrical shell in directions α, β and γ, respectively.

$$\left.\begin{array}{l} \frac{\partial F_{T1}}{\partial\alpha} + \frac{\partial F_{T12}}{\partial\beta} + q_1 = 0 \\ \frac{\partial F_{T2}}{\partial\beta} + \frac{\partial F_{T21}}{\partial\alpha} + q_2 = 0 \\ -\frac{F_{T2}}{R} + \frac{\partial F_{S1}}{\partial\alpha} + \frac{\partial F_{S2}}{\partial\beta} + q_3 = 0 \\ \frac{\partial M_{12}}{\partial\beta} + \frac{\partial M_1}{\partial\alpha} - F_{S1} = 0 \\ \frac{\partial M_{21}}{\partial\alpha} + \frac{\partial M_2}{\partial\beta} - F_{S2} = 0 \end{array}\right\} \quad (10)$$

The geometric equations of the cylindrical shell are shown in Equation (11), as follows. In Equation (11), R represents the radius of the middle face of the cylindrical shell; ε_1 and ε_2 represent the normal strains along the directions α and β on the middle face of the cylindrical shell, respectively; ε_{12} and ε_{21} represent the shear strains along the directions α and β on the middle face of the cylindrical shell, respectively; χ_1 and χ_2 represent the change of the main curvature of each point along the directions α and β on the middle face of the cylindrical shell, respectively; χ_{12} and χ_{21} represent the change of the twisting curvature of each point along the directions α and β on the middle face of the cylindrical shell, respectively; and u, v and w represent the displacement of the cylindrical shell in the directions α, β and γ, respectively.

$$\left.\begin{array}{l}\varepsilon_1 = \frac{\partial u}{\partial \alpha} \\ \varepsilon_2 = \frac{\partial v}{\partial \beta} + \frac{w}{R} \\ \varepsilon_{12} = \varepsilon_{21} = \frac{\partial u}{\partial \beta} + \frac{\partial v}{\partial \alpha} \\ \chi_1 = -\frac{\partial^2 w}{\partial \alpha^2} \\ \chi_2 = -\frac{\partial^2 w}{\partial \beta^2} \\ \chi_{12} = \chi_{21} = -\frac{\partial^2 w}{\partial \alpha \partial \beta}\end{array}\right\} \tag{11}$$

The physical equations of the cylindrical shell are shown in Equation (12) below. In Equation (12), E represents Young's modulus; μ represents Poisson's ratio; δ represents the thickness of cylindrical shell; D represents the bending stiffness of the cylindrical shell, and $D = \frac{E\delta^3}{12(1-\mu^2)}$. The other symbols are the same as before.

$$\left.\begin{array}{l}F_{T1} = \frac{E\delta}{1-\mu^2}(\varepsilon_1 + \mu\varepsilon_2) \\ F_{T2} = \frac{E\delta}{1-\mu^2}(\varepsilon_2 + \mu\varepsilon_1) \\ F_{T12} = F_{T21} = \frac{E\delta}{2(1+\mu)}\varepsilon_{12} \\ M_1 = D(\chi_1 + \mu\chi_2) \\ M_2 = D(\chi_2 + \mu\chi_1) \\ M_{12} = M_{21} = (1-\mu)D\chi_{12}\end{array}\right\} \tag{12}$$

From the equilibrium differential equations, geometric equations, and physical equations above, it can be determined that there are eight internal forces but only three displacements in the bending problem of the cylindrical shell, so it will be easier to use the displacement method to solve it. In order to obtain the equilibrium differential equations of the cylindrical shell, represented by the displacements in the displacement method, it is first necessary to substitute the geometric equations into the physical equations; thus, Equation (11) is substituted into Equation (12) to obtain the elastic equations, as shown in Equation (13). The last three equations in Equation (13) are substituted into the last two equations in Equation (10), and then Equation (14) will be obtained as follows. In Equation (14), $\nabla^2 = \frac{\partial^2}{\partial \alpha^2} + \frac{\partial^2}{\partial \beta^2}$, and the other symbols are the same as before. Finally, Equations (13) and (14) are substituted into the first three equations of Equation (10) to obtain the equilibrium differential equations of the cylindrical shell expressed by the displacements of the middle face, which are the basic equilibrium differential equations solving the bending problem of the cylindrical shell by the displacement method, as shown in Equation (15).

$$\left.\begin{array}{l}F_{T1} = \frac{E\delta}{1-\mu^2}\left[\frac{\partial u}{\partial \alpha} + \mu\left(\frac{\partial v}{\partial \beta} + \frac{w}{R}\right)\right] \\ F_{T2} = \frac{E\delta}{1-\mu^2}\left[\left(\frac{\partial v}{\partial \beta} + \frac{w}{R}\right) + \mu\frac{\partial u}{\partial \alpha}\right] \\ F_{T12} = F_{T21} = \frac{E\delta}{2(1+\mu)}\left(\frac{\partial u}{\partial \beta} + \frac{\partial v}{\partial \alpha}\right) \\ M_1 = -D\left(\frac{\partial^2 w}{\partial \alpha^2} + \mu\frac{\partial^2 w}{\partial \beta^2}\right) \\ M_2 = -D\left(\frac{\partial^2 w}{\partial \beta^2} + \mu\frac{\partial^2 w}{\partial \alpha^2}\right) \\ M_{12} = M_{21} = -(1-\mu)D\frac{\partial^2 w}{\partial \alpha \partial \beta}\end{array}\right\} \tag{13}$$

$$\left.\begin{array}{l}F_{S1} = -D\frac{\partial}{\partial \alpha}\nabla^2 w \\ F_{S2} = -D\frac{\partial}{\partial \beta}\nabla^2 w\end{array}\right\} \tag{14}$$

$$\left.\begin{array}{c}\left(\frac{\partial^2}{\partial \alpha^2} + \frac{1-\mu}{2}\frac{\partial^2}{\partial \beta^2}\right)u + \frac{1+\mu}{2}\frac{\partial^2 v}{\partial \alpha \partial \beta} + \frac{\mu}{R}\frac{\partial w}{\partial \alpha} = -\frac{1-\mu^2}{E\delta}q_1 \\ \frac{1+\mu}{2}\frac{\partial^2 u}{\partial \alpha \partial \beta} + \left(\frac{\partial^2}{\partial \beta^2} + \frac{1-\mu}{2}\frac{\partial^2}{\partial \alpha^2}\right)v + \frac{1}{R}\frac{\partial w}{\partial \beta} - \frac{1}{R^2}\frac{\mathrm{d}R}{\mathrm{d}\beta}w = -\frac{1-\mu^2}{E\delta}q_2 \\ \frac{\mu}{R}\frac{\partial u}{\partial \alpha} + \frac{1}{R}\frac{\partial v}{\partial \beta} + \frac{w}{R^2} + \frac{\delta^2}{12}\nabla^4 w = \frac{1-\mu^2}{E\delta}q_3\end{array}\right\} \tag{15}$$

4.2. Internal Force Expressions of Circular Cylindrical Shell

Equation (15) is very difficult to solve because the coefficients include R and $\frac{dR}{d\beta}$, which are usually functions of β, so the equilibrium differential equations are not constant coefficients but variable coefficients. However, if the middle face is set to a circular cylindrical surface, the cylindrical shell will be a circular cylindrical shell, and as a result R will become a constant and $\frac{dR}{d\beta}$ will become 0. Therefore, the equilibrium differential Equation (15) variable coefficients become differential equations with constant coefficients, which are relatively easy to solve. The circular diaphragm wall of the north anchorage foundation pit in the engineering case can be approximately simplified into a thin circular cylindrical shell model. Moreover, it has been noted that the loads applied on the circular diaphragm wall are mainly in the horizontal direction (the normal direction) in the excavation process of the foundation pit, and the impact of the loads in other directions is slight; as a consequence, the loads in other directions can be ignored. Thus, Equation (15) can be further simplified to derive the basic equilibrium differential equations of the circular cylindrical shell under only a normal load, as shown in Equation (16).

$$\left.\begin{array}{c}\left(\frac{\partial^2}{\partial\alpha^2}+\frac{1-\mu}{2}\frac{\partial^2}{\partial\beta^2}\right)u+\frac{1+\mu}{2}\frac{\partial^2 v}{\partial\alpha\partial\beta}+\frac{\mu}{R}\frac{\partial w}{\partial\alpha}=0\\ \frac{1+\mu}{2}\frac{\partial^2 u}{\partial\alpha\partial\beta}+\left(\frac{\partial^2}{\partial\beta^2}+\frac{1-\mu}{2}\frac{\partial^2}{\partial\alpha^2}\right)v+\frac{1}{R}\frac{\partial w}{\partial\beta}=0\\ \frac{\mu}{R}\frac{\partial u}{\partial\alpha}+\frac{1}{R}\frac{\partial v}{\partial\beta}+\frac{w}{R^2}+\frac{\delta^2}{12}\nabla^4 w=\frac{1-\mu^2}{E\delta}q_3\end{array}\right\} \tag{16}$$

By introducing the displacement function $H = H(\alpha, \beta)$, the displacements of the middle face can be expressed as Equation (17).

$$\left.\begin{array}{c}u=\frac{\partial}{\partial\alpha}\left(\frac{\partial^2}{\partial\beta^2}-\mu\frac{\partial^2}{\partial\alpha^2}\right)H\\ v=-\frac{\partial}{\partial\beta}\left[\frac{\partial^2}{\partial\beta^2}+(2+\mu)\frac{\partial^2}{\partial\alpha^2}\right]H\\ w=R\nabla^4 H\end{array}\right\} \tag{17}$$

Then, the first two equations of Equation (11) can be always satisfied, while the third equation must be satisfied with Equation (18).

$$\nabla^8 H+\frac{E\delta}{R^2 D}\frac{\partial^4 H}{\partial\alpha^4}=\frac{q_3}{RD} \tag{18}$$

Then, the internal forces expressed by the displacement function H can be obtained by substituting Equation (17) into Equations (13) and (14), producing Equation (19), as follows. Thus, the boundary conditions can always be expressed by H, and H can be solved from Equation (18) in the boundary conditions. Then, the displacements of the middle face can be solved from Equation (17), and the internal forces can be obtained from Equation (19).

$$\left.\begin{array}{l}F_{T1}=E\delta\frac{\partial^4 H}{\partial\alpha^2\partial\beta^2}\\ F_{T2}=E\delta\frac{\partial^4 H}{\partial\alpha^4}\\ F_{T12}=F_{T21}=-E\delta\frac{\partial^4 H}{\partial\alpha^3\partial\beta}\\ M_1=-RD\left(\frac{\partial^2}{\partial\alpha^2}+\mu\frac{\partial^2}{\partial\beta^2}\right)\nabla^4 H\\ M_2=-RD\left(\frac{\partial^2}{\partial\beta^2}+\mu\frac{\partial^2}{\partial\alpha^2}\right)\nabla^4 H\\ M_{12}=M_{21}=-(1-\mu)RD\frac{\partial^2}{\partial\alpha\partial\beta}\nabla^4 H\\ F_{S1}=-RD\frac{\partial}{\partial\alpha}\nabla^6 H\\ F_{S2}=-RD\frac{\partial}{\partial\beta}\nabla^6 H\end{array}\right\} \tag{19}$$

4.3. Internal Force Expressions of Circular Cylindrical Shell under Normal Loads

When a circular cylindrical shell is only subjected to normal load $q_3 = q_3(\alpha)$, which is symmetric about the central axis of the circular cylindrical shell, and the boundaries are also symmetric about the central axis, the displacements and internal forces will also be symmetric about the central axis and their expressions will only be the functions of α. In this case, the displacement function H can be set as a function including independent variable α only, $H = H(\alpha)$, and the partial differential Equation (18) can be simplified to the ordinary differential Equation (20).

$$\nabla^8 H + \frac{E\delta}{R^2 D}\frac{\partial^4 H}{\partial \alpha^4} = \frac{q_3}{RD} \tag{20}$$

Accordingly, the third equation in Equation (17) can be simplified as Equation (21).

$$w = R\frac{\mathrm{d}^4 H}{\mathrm{d}\alpha^4} \tag{21}$$

Equation (22) can be derived through substituting Equation (21) into Equation (20). Equation (22) is a fourth-order ordinary differential equation for w, which can be solved according to two boundary conditions on w at each boundary.

$$\frac{\mathrm{d}^4 w}{\mathrm{d}\alpha^4} + \frac{E\delta}{R^2 D}w = \frac{q_3}{D} \tag{22}$$

By using Equation (21) and $H = H(\alpha)$, the Equation (23) of internal forces can be obtained from Equation (19), so that all internal forces can be calculated from the solution of w.

$$\left.\begin{array}{l} F_{\mathrm{T1}} = 0 \\ F_{\mathrm{T2}} = \frac{E\delta}{R}w \\ F_{\mathrm{T12}} = F_{\mathrm{T21}} = 0 \\ M_1 = -D\frac{\mathrm{d}^2 w}{\mathrm{d}\alpha^2} \\ M_2 = -\mu D\frac{\mathrm{d}^2 w}{\mathrm{d}\alpha^2} = \mu M_1 \\ M_{12} = M_{21} = 0 \\ F_{\mathrm{S1}} = -D\frac{\mathrm{d}^3 w}{\mathrm{d}\alpha^3} \\ F_{\mathrm{S2}} = 0 \end{array}\right\} \tag{23}$$

In order to simplify the solution, a constant λ is cited that is expressed as Equation (24) with a dimension of L^{-1}.

$$\lambda = \left(\frac{E\delta}{4R^2 D}\right)^{\frac{1}{4}} = \left[\frac{3(1-\mu^2)}{R^2\delta^2}\right]^{\frac{1}{4}} \tag{24}$$

Then, one coordinate ξ with a dimension of 1 is cited instead of α.

$$\xi = \lambda\alpha \tag{25}$$

Thus, the differential Equation (22) is transformed into Equation (26), as follows.

$$\frac{\mathrm{d}^4 w}{\mathrm{d}\xi^4} + 4w = \frac{4R^2}{E\delta}q_3 \tag{26}$$

Consequently, the solution to Equation (26) can be obtained as Equation (27).

$$w = C_1 \sin\xi\sinh\xi + C_2 \sin\xi\cos\mathrm{h}\xi + C_3 \cos\xi\sinh\xi + C_4 \cos\xi\cosh\xi + w_0 \tag{27}$$

In Equation (27), w_0 is any one particular solution, which can be selected by the function form of the normal load according to the requirements of differential Equation (26).

The constants of C_1, C_2, C_3 and C_4 are determined by the boundary conditions, and Equation (23) of internal forces could be further transformed into Equation (28).

$$\left.\begin{array}{l} F_{T1} = 0 \\ F_{T2} = \frac{E\delta}{R} w \\ F_{T12} = F_{T21} = 0 \\ M_1 = -\lambda^2 D \frac{d^2 w}{d\xi^2} \\ M_2 = -\mu\lambda^2 D \frac{d^2 w}{d\xi^2} = \mu M_1 \\ M_{12} = M_{21} = 0 \\ F_{S1} = -\lambda^3 D \frac{d^3 w}{d\xi^3} \\ F_{S2} = 0 \end{array}\right\} \quad (28)$$

4.4. Solving Steps

For the engineering case in this study, the circular diaphragm wall of the north anchorage foundation pit is subjected to four normal loads: the horizontal supporting force q_M of the cap beam, the horizontal supporting force q_{Ci} of the lining, the horizontal subgrade reaction $e_p(\alpha)$ on the pit-facing surface of the circular diaphragm wall, and the horizontal earth pressure strengths e_{an} and e'_{an} on the pit-back surface of the circular diaphragm wall. According to the circular cylindrical shell theory above and the superposition principle in elasticity, the solving steps for deriving the results of the circular diaphragm wall under normal loads in every working condition in the engineering case can be concluded as follows.

Firstly, all four normal loads in every working condition must be calculated, including q_M, q_{Ci}, $e_p(\alpha)$, e_{an} and e'_{an}.

Secondly, the internal forces and deformations A_i, B_i, C_i, D_i of the circular diaphragm wall, caused by each normal load in any one working condition, should be calculated by Equation (29).

$$\left.\begin{array}{c} A_i = f(q_M) \\ B_i = f(q_{Ci}) \\ C_i = f[e_p(\alpha)] \\ D_i = f[e_{an}, e'_{an}] \end{array}\right\} \quad (29)$$

Finally, the total internal force and deformation F_i will be obtained in each working condition by Equation (30).

$$F_i = A_i + B_i + C_i + D_i \quad (30)$$

5. Finite Element Numerical Simulation Method (FENSM)

Based on the project profile, considering the influence of various factors such as arch effect and rock-socketed depth, a three-dimensional continuum model was established with the finite element software that included the cap beam, lining, diaphragm wall and surrounding soil, as shown in Figure 5, so that the mechanical responses of the diaphragm wall, which included the radial displacement, circumferential stress and vertical bending moment, could be determined during excavation. As for whether the three-dimensional continuum finite element model can reflect the circular arch effect of the circular diaphragm wall effectively and obtain reliable calculation results, this should be verified later by comparing with the SMR.

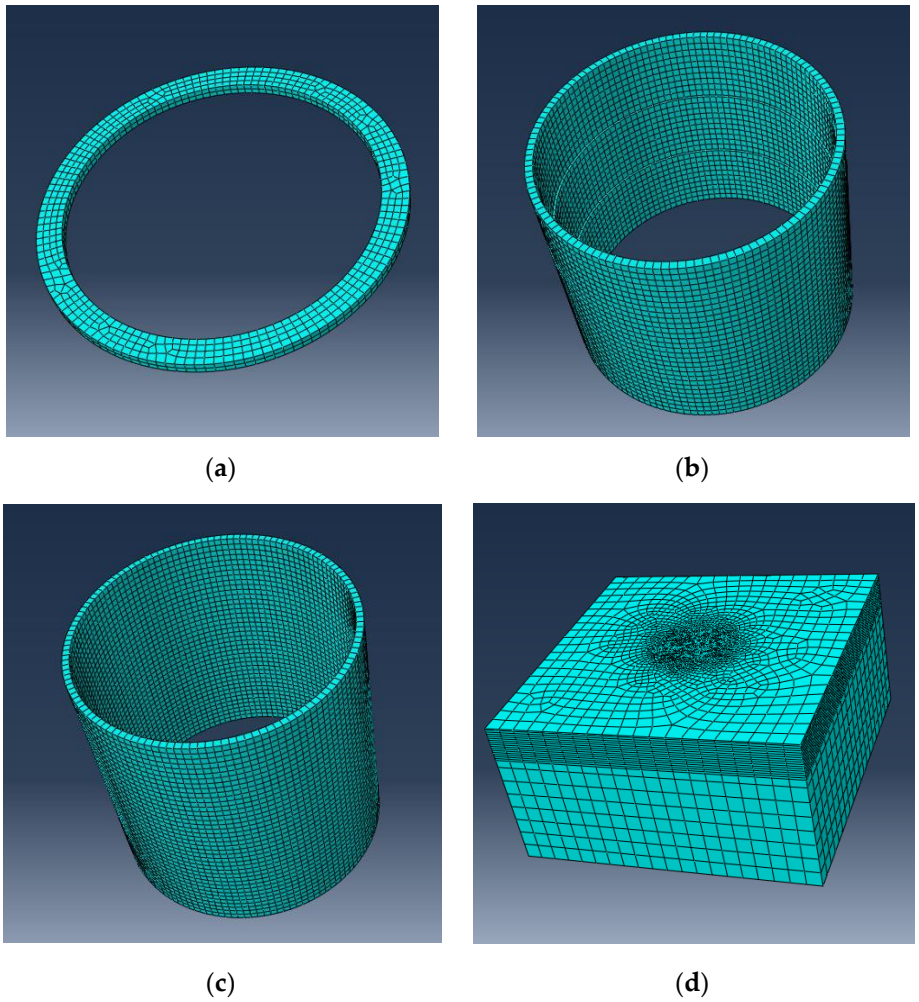


Figure 5. Three-dimensional continuum finite element mesh models. (**a**) Cap beam. (**b**) Lining. (**c**) Circular diaphragm wall. (**d**) Soil.

5.1. Establishment of Mesh Model

The mesh models of the cap beam, lining and circular diaphragm wall were built according to their actual sizes with the eight-node hexahedral solid unit (C3D8R) and elastic material. The cap beam was divided into 1024 units with 1926 nodes, the lining was divided into 7800 units with 12,220 nodes, and the circular diaphragm wall was divided into 5200 units with 10,660 nodes. The specific mesh models are shown in Figure 5.

As shown in Figure 5d, the mesh model of soil was built with the eight-node hexahedral solid unit (C3D8R) and elastoplastic material conforming to the Mohr–Coulomb yielding criteria. Considering the size of the circular foundation pit, the length, width and height of the soil model were set as 400 m, 400 m and 200 m, respectively, with 88,272 units and 92,975 nodes. The detailed physical and mechanical parameters were set according to Table 2.

5.2. Application of Boundary Conditions and Loads

As shown in Figure 6, for the overall modeling, the bottom of the model was set as full constraint ($U_x = U_y = U_z = 0$); the two surfaces in the normal direction x were limited by the displacement in the direction x ($U_x = 0$); the two surfaces in the normal direction y were limited by the displacement in the direction y ($U_y = 0$); and the upper surface of the model was set as a free surface. The boundary conditions of the model are shown in Figure 6.

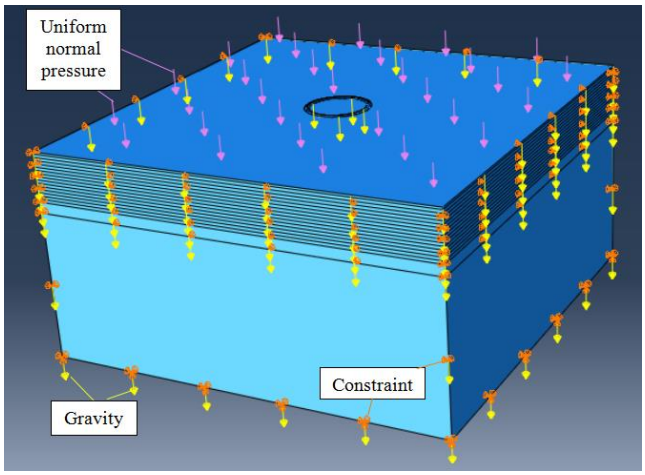


Figure 6. Boundary conditions and loads on the model.

In addition to the gravity of the model, the gravity of the overlying soil layer with a thickness of 4.14 m, the random construction loads, and the vehicles loads around the foundation pit should also be considered for the loads on the model during the excavation. In summary, a uniform normal pressure of 80 kPa was applied to the soil model upper surface.

5.3. Simulation of Construction Process

The construction process of the foundation pit in the numerical simulation was consistent with the actual construction situation in Table 1, but the detailed excavation process of the soil and the detailed reinforced concrete construction process of the lining were not considered. This study was mainly concerned with the safety and stability of the supporting structure in pit excavation; the numerical simulation was only carried out until the completion of the soil excavation and the lining construction; and the construction of the foundation plate and later the relatively safe construction phase were no longer simulated. The "passivate" and "activate" functions of regional units in the software were used to hide the soil units and regenerate the lining units layer by layer, respectively, so as to simulate the foundation pit construction process. A total of 36 analysis steps were set and the specific working condition of each analysis step was established according to Table 1.

6. Site Monitoring

For the mechanical responses of the circular foundation pit in the excavation, it is difficult to obtain accurate results through theoretical calculation and numerical simulation. Even using the model test, it is also difficult to simulate the complex geological, hydrological, load and other site conditions, and the test results may not be able to reflect the actual situation of circular foundation pit truthfully in the excavation; therefore, site monitoring with dynamic monitoring feedback is very important. In essence, site monitoring of the circular foundation pit is equivalent to an equal scale model test at 1:1, and the monitoring data obtained are relatively accurate, which is a reliable basis for confirming the results of the theoretical calculation and numerical simulation.

In order to verify the correctness of the TCR and NSR, the monitoring process and results of the section at Point A (hereinafter referred to as Section A) of the circular diaphragm wall were selected as references according to the centrosymmetry property, and the specific location of Point A is shown in Figure 7. Two monitoring items were mainly carried out, including the radial displacement monitoring and circumferential stress monitoring of Section A, and the vertical bending moments of Section A could be obtained by the difference method from the results of the radial displacement monitoring [31].

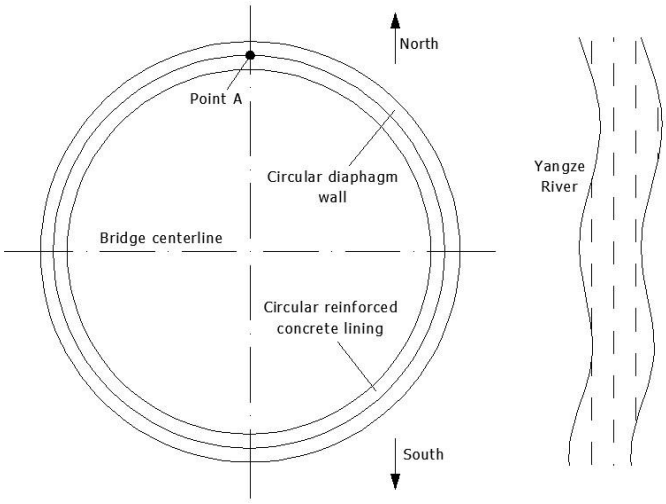


Figure 7. The position of Point A.

6.1. Radial Displacement Monitoring

The radial displacement monitoring was to monitor the deep horizontal displacement of the circular diaphragm wall at Section A, and the instruments required included the movable vertical clinometer, the readout instrument for clinometer, and the pipe for the clinometer, as shown in Figure 8. From Figure 8a, we can see that the movable vertical clinometer consisted of the probe and cable. The probe was equipped with a high-precision accelerometer, which had good sealing performance and could withstand certain water pressure. There were two sets of guide wheels on the upper and lower parts of the probe, to facilitate its lifting and sliding along the guide slots in the pipe. The cable, besides powering and transmitting signals to the internal accelerometer, was able to connect the probe to the readout instrument and serve as a scale for the probe test point and a rope for the probe rising and falling. There was a mark on the cable every 0.5 m and the distance is indicated by amark that started from the middle point of the two sets of guide wheels. As shown in Figure 8b, the readout instrument for the clinometer was composed of the display, working power supply, power switch and other devices. As shown in Figure 8c, the pipe for the clinometer was made of PVC material, with a diameter of 70 mm and a length of 2 m for each one. An entire pipe was formed at Section A by connecting each pipe together, and the top of the entire pipe should be 20 cm long over the cap beam. There were two pairs of orthogonal longitudinal guide slots in the pipe, and the probe guide wheels were located in a pair of guide slots during measurement to ensure they could slide up and down freely. When the reinforcement cage of the circular diaphragm wall was made, the enter pipe was fixed on the reinforcement cage and then placed in the right position, with the reinforcement cage being placed into the excavated slot. The pipe must be protected when the concrete of the circular diaphragm wall is poured, and its perpendicularity must also be ensured. The specific position of the pipe in the circular diaphragm wall after installation is shown in Figure 2, and the monitoring frequency of radial displacement in the construction process is shown in Table 3.

Table 3. Monitoring frequency.

Monitoring Item	Monitoring Frequency		
	Excavation 0 m~15 m	**Excavation 15 m~30 m**	**Excavation 30 m~45 m**
Radial displacement monitoring	Once/3 d	Once/2 d	Once/d
Circumferential stress monitoring	Once/3 d	Once/2 d	Once/d



(**a**) (**b**) (**c**)

Figure 8. Instruments for radial displacement monitoring. (**a**) Movable vertical clinometer. (**b**) Readout instrument for clinometer. (**c**) Pipe for clinometer.

6.2. Circumferential Stress Monitoring

Firstly, the circumferential stress monitoring was to monitor the concrete circumferential strain of the circular diaphragm wall at Section A, and then the circumferential strain could be converted to the circumferential stress according to the generalized Hooke's law. The used instruments included the vibrating string concrete strain gauge and frequency readout instrument as shown in Figure 9. As shown in Figure 2, the concrete strain gauges were bound at the three monitoring points at Section A, along the circumferential direction on the reinforced cage, and the distances between the monitoring points and the top of circular diaphragm wall from top to bottom are 14 m, 29 m and 44 m, successively. In order to prevent the failure of the monitoring points for the damage of strain gauges and ensure the accuracy of monitoring, two strain gauges were arranged at every monitoring point. The frequency readout instrument was used to read the data, and the average of the two strain gauges was taken as the final strain value for each monitoring point. The monitoring frequency of circumferential stress in the construction process is shown in Table 3.



(**a**) (**b**) (**c**)

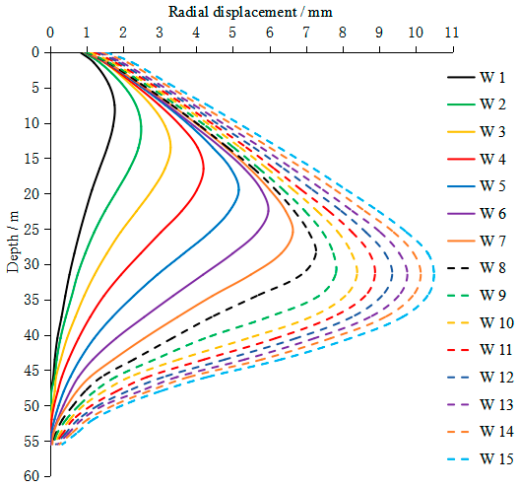
Figure 9. Instruments for circumferential stress monitoring. (**a**) Concrete strain gauge. (**b**) Frequency readout instrument. (**c**) Binding of concrete strain gauge.

7. Results and Discussion

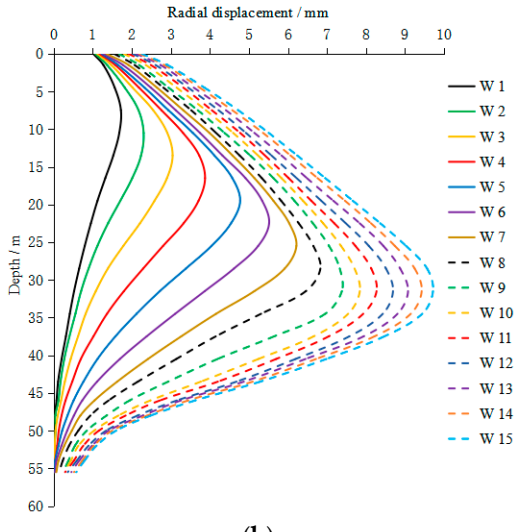
Based on the project background, the proposed CCSTCM and FENSM were adopted to calculate the radial displacement, circumferential stress and vertical bending moment of the circular diaphragm wall, and the TCR and NSR were obtained. In order to prove the correctness of the TCR and NSR and the applicability of the CCSTCM and FENSM, by combining with the site monitoring position, the TCR, NSR and SMR at Section A were

compared and analyzed. The following items need to be explained for discussing the results clearly.

(1) W 1~W 15 in Figures 10–12 represent, respectively, the working conditions of the layers of soil, which have been excavated completely but the corresponding lining has not been constructed.
(2) The 0 on the vertical axis in Figures 10–12 represents the position of the top surface of the circular diaphragm wall.
(3) The radial displacement and vertical bending moment in Figures 10 and 12 are prescribed a plus for the inner of the foundation pit and a minus for the outside.
(4) The values of radial displacement, circumferential stress and vertical bending moment are only distinguished by the absolute values without considering plus and minus when describing the change law of the curve.

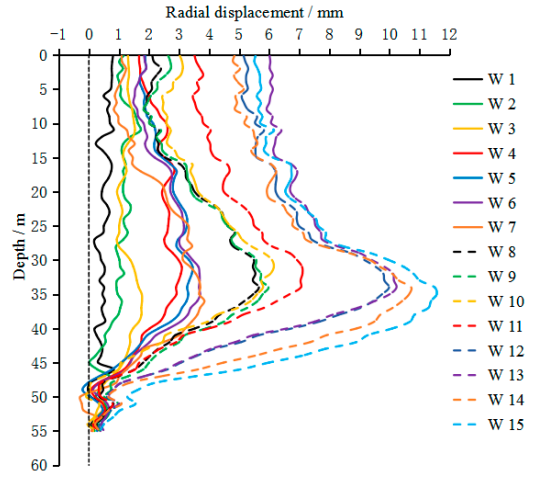


(**a**)

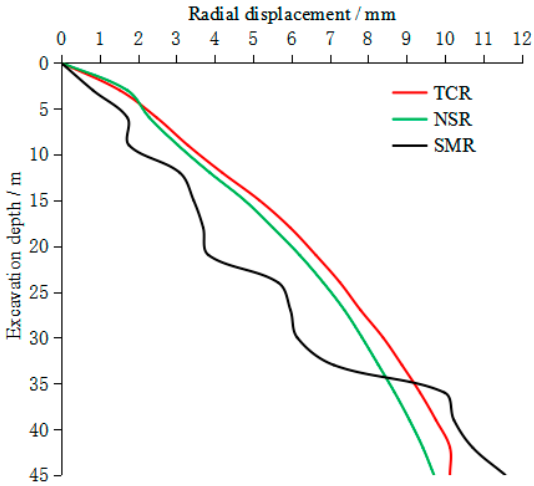


(**b**)

Figure 10. *Cont.*

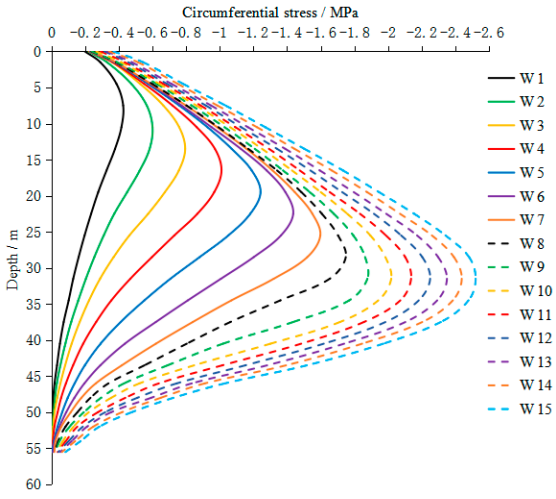


(**c**)



(**d**)

Figure 10. Radial displacement results of the circular diaphragm wall at Point A. (**a**) Variation of radial displacements obtained by CCSTCM with depth in different working conditions. (**b**) Variation of radial displacements obtained by FENSM with depth in different working conditions. (**c**) Variation of radial displacements obtained by site monitoring with depth in different working conditions. (**d**) Variation of maximum radial displacements with excavation depth.



(**a**)

Figure 11. *Cont.*

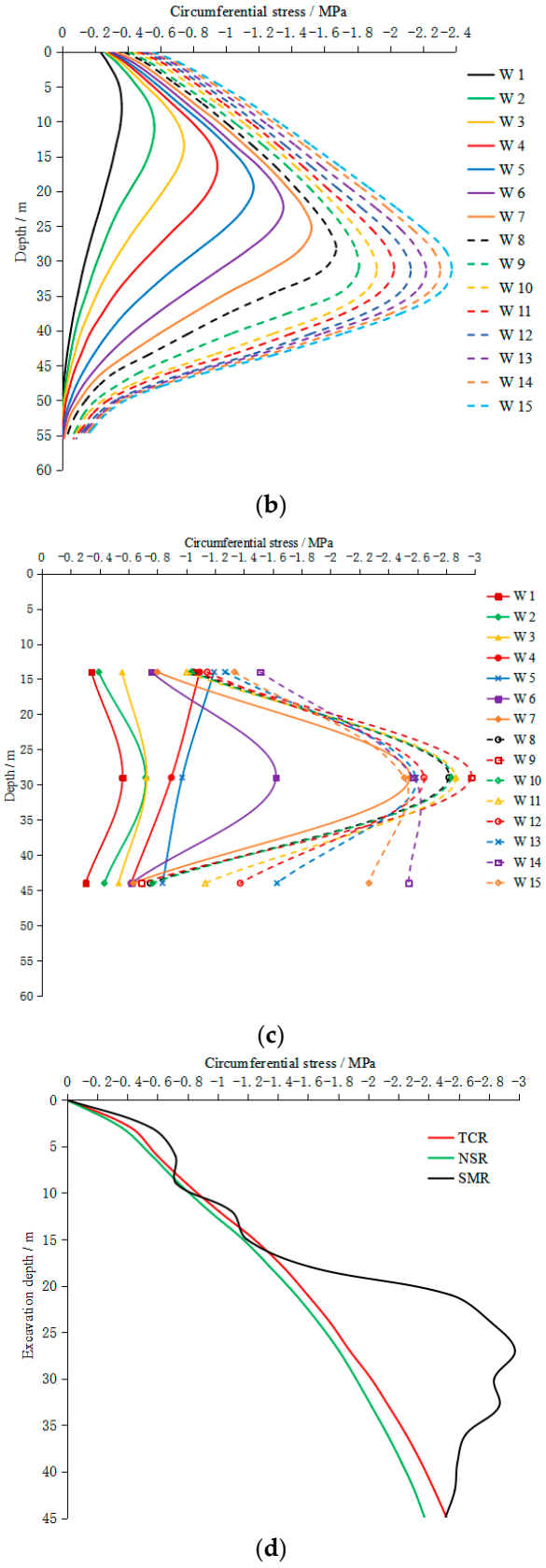
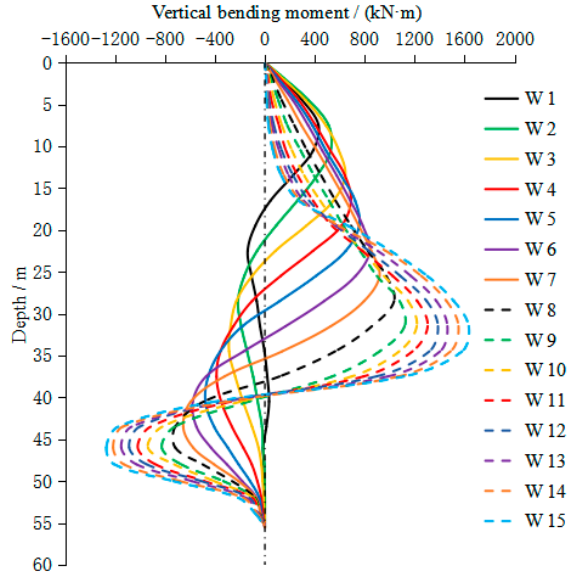
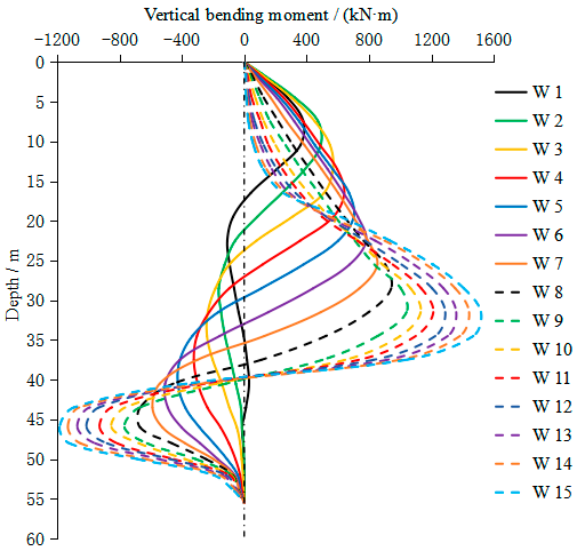


Figure 11. Circumferential stresses results of the circular diaphragm wall at Point A. (**a**) Variation of circumferential stresses obtained by CCSTCM with depth in different working conditions. (**b**) Variation of circumferential stresses obtained by FENSM with depth in different working conditions. (**c**) Variation of circumferential stresses obtained by site monitoring with depth in different

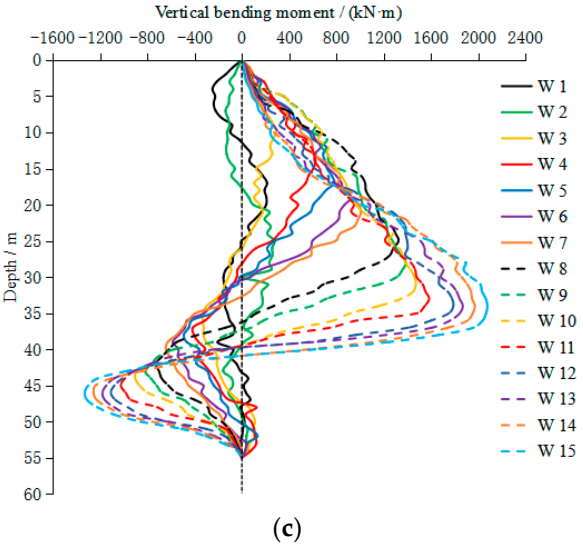
working conditions. (**d**) Variation of maximum circumferential stresses with excavation depth.



(**a**)

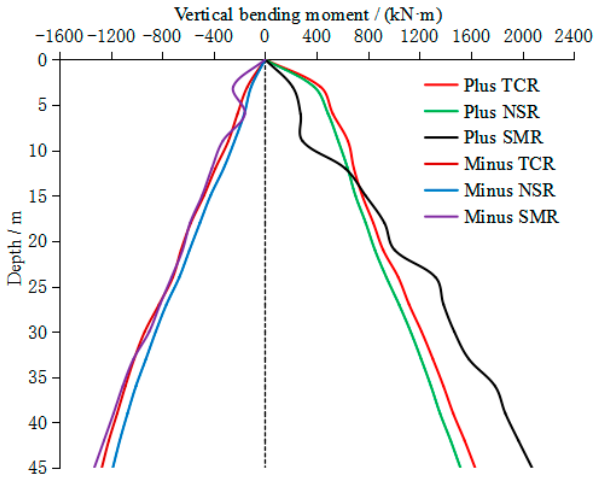


(**b**)



(**c**)

Figure 12. *Cont*.



(**d**)

Figure 12. Vertical bending moment results of the circular diaphragm wall at Point A. (**a**) Variation of vertical bending moments obtained by CCSTCM with depth in different working conditions. (**b**) Variation of vertical bending moments obtained by FENSM with depth in different working conditions. (**c**) Variation of vertical bending moments obtained by site monitoring with depth in different working conditions. (**d**) Variation of maximum vertical bending moments with excavation depth.

7.1. Radial Displacement of Circular Diaphragm Wall

The radial displacements of the circular diaphragm wall obtained through the CCSTCM, FENSM and site monitoring are shown in Figure 10. From Figure 10, we can observe that the radial displacements of the circular diaphragm wall obtained through both the CCSTCM and FENSM increase first and then decrease with the increase in depth in different working conditions. The maximum radial displacement increases gradually with the increase in excavation depth, and the position of the maximum radial displacement declines gradually and then tends to be stable with the increase in excavation depth. The TCR values are slightly larger than the NSR values. Except for Working Conditions 1 and 2 (W 1 and W 2), in other working conditions, the radial displacements of the circular diaphragm wall obtained from site monitoring increase first and then basically decrease with the increase in depth. The maximum radial displacement increases gradually with the increase in excavation depth, but there are obvious fluctuations. The position of the maximum radial displacement gradually declines with the increase in excavation depth and then also tends to be stable. Combined with Table 4, it can be further determined that the extremum of the maximum radial displacements obtained from the field monitoring is 11.6 mm, which occurs 35 m from the top of the circular diaphragm wall in the last working condition (W 15). The extremum of the maximum radial displacements obtained from the CCSTCM is 10.1 mm, which is 87.1% of the SMR and occurs 32 m from the top of the circular diaphragm wall in W 15. The extremum of the maximum radial displacements obtained from the FENSM is 9.7 mm, which is 83.6% of the SMR and 96.0% of the TCR, and occurs 32 m from the top of the circular diaphragm wall in W 15 also. Generally speaking, the variation rules of the radial displacements obtained by the three methods are basically the same, and the curves of the radial displacements show the shape of "big in the middle and small at both ends"; however, the SMR are slightly larger than the TCR and NSR and closer to the TCR. To a certain extent, the proposed CCSTCM and the numerical calculation model established are reasonable. Because all the maximum radial displacements of circular diaphragm wall obtained by the three methods are generated at the last working condition and the depth range is about 31 m~36 m, the reinforcement measures should be taken within this depth range when the excavation of the north anchorage foundation pit reaches the last several working conditions.

Table 4. The extremum comparison of the results.

Method	EMRD	PCS /%	P /m	EMCS /Mpa	PCS /%	P /m	EMVPBM /kN·m	PCS /%	P /m	EMVMBM /kN·m	PCS /%	P /m
Site monitoring	11.6	-	35	2.973	-	29	2074.5	-	34	−1328.1	-	46
CCSTCM	10.1	87.1	32	2.521	84.8	32	1632.2	78.7	32	−1269.8	95.6	46
FENSM	9.7	83.6	32	2.375	79.9	32	1518.0	73.2	32	−1183.9	89.1	46

Note: EMRD represents the extremum of the maximum radial displacements; P represents the position of the extremum; EMCS represents the extremum of the maximum circumferential stresses; EMVPBM represents the extremum of the maximum vertical plus bending moment; EMVMBM represents the extremum of the maximum vertical minus bending moment; PCS represents the percentage compared with the SMR.

7.2. Circumferential Stress of Circular Diaphragm Wall

The circumferential stresses of the circular diaphragm wall obtained through the CCSTCM, FENSM and site monitoring are shown in Figure 11, and they are minus, which represents compressive stress. From Figure 11, we can observe that the circumferential stresses of the circular diaphragm wall obtained through both the CCSTCM and FENSM increase first and then decrease with the increase in depth in different working conditions. The maximum circumferential stress increases gradually with the increase in excavation depth, and the position of the maximum circumferential stress declines gradually and then tends to be stable with the increase in excavation depth. The TCR values are slightly larger than the NSR values. Except for Working Conditions 4 and 5 (W 4 and W 5), in other working conditions, the circumferential stresses of the circular diaphragm wall obtained from the site monitoring increase first and then basically decrease with the increase in depth. The maximum circumferential stress increases first and then decreases slightly with the increase in excavation depth, but the fluctuations are obvious. Combined with Table 4, it can be further determined that the extremum of the circumferential stresses obtained from the site monitoring is 2.973 Mpa, which occurs 29 m from the top of the circular diaphragm wall in the ninth working condition (W 9). The extremum of the maximum circumferential stresses obtained from the CCSTCM is 2.521 Mpa, which is 84.8% of the SMR and occurs 32 m from the top of the circular diaphragm wall in W 15. The extremum of the maximum circumferential stresses obtained from the FENSM is 2.375 Mpa, which is 79.9% of the SMR and 94.2% of the TCR, and occurs 32 m from the top of the circular diaphragm wall in W 15 also. Generally speaking, the variation rules of the circumferential stresses obtained by the three methods are the same and basically in accordance with those of the radial displacements, and the SMR values are slightly larger than the TCR and NSR values and closer to the TCR values, which further illustrates that the proposed CCSTCM and the numerical calculation model established are reasonable and applicable. However, the extremum of the maximum circumferential stresses obtained from the site monitoring occurs 29 m from the top of the circular diaphragm wall in W 9, which is quite different from the position and working conditions of the extremum of the maximum radial displacements. The reason for this could be related to many factors, such as the perpendicularity deviation of the wall, the thickness deviation of the wall, or the mud added to the joint in the actual construction process of the circular diaphragm wall. Another possibility is that the monitoring points of the circumferential stress set were insufficient at Section A, so there was a certain deviation for the TCR.

7.3. Vertical Bending Moment of Circular Diaphragm Wall

The vertical bending moments of the circular diaphragm wall obtained through the CCSTCM, FENSM and site monitoring are shown in Figure 12. From Figure 12, we can observe that the vertical bending moments of the circular diaphragm wall obtained through both the CCSTCM and FENSM increase first to the maximum vertical plus bending moments, then to the maximum vertical minus bending moments, and finally decrease to 0 with the increase in depth in different working conditions. The maximum vertical plus bending moments and maximum vertical minus bending moments increase gradually with the increase in excavation depth, and the positions of the maximum vertical plus bending

moments and maximum vertical minus bending moments decline gradually and then tend to be stable with the increase in excavation depth. The TCR are slightly larger than the NSR. Except for Working Conditions 1 and 2, in other working conditions, the vertical bending moments of the circular diaphragm wall obtained through the site monitoring first increase to the maximum vertical plus bending moments, then to the maximum vertical minus bending moments, and finally decrease to 0 with the increase in depth. The maximum vertical plus bending moments and maximum vertical minus bending moments increase gradually with the increase in excavation depth, and the positions of the maximum vertical plus bending moments and maximum vertical minus bending moments decline gradually and then tend to be stable with the increase in excavation depth. Combined with Table 4, it can be further determined that the extremum of the maximum vertical plus bending moments obtained from the site monitoring is 2074.5 kN·m, which occurs 34 m from the top of the circular diaphragm wall in W 15. The extremum of the maximum vertical plus bending moments obtained from the CCSTCM is 1632.2 kN·m, which is 78.7% of the SMR, and occurs 32 m from the top of the circular diaphragm wall in W 15. The extremum of the maximum vertical plus bending moments obtained from the FENSM is 1518.0 kN·m, which is 73.2% of the SMR and 93.0% of the TCR, occurs 32 m from the top of the circular diaphragm wall in W 15 also. The extremum of the maximum vertical minus bending moments obtained from the site monitoring is −1328.1 kN·m, which occurs 46 m from the top of the circular diaphragm wall in W 15. The extremum of the maximum vertical minus bending moments obtained from the CCSTCM is −1269.8 kN·m, which is 95.6% of the SMR, and occurs 46 m from the top of the circular diaphragm wall in W 15. The extremum of the maximum vertical minus bending moments obtained from the FENSM is −1183.9 kN·m, which is 89.1% of the SMR and 93.2% of the TCR, occurs 46 m from the top of the circular diaphragm wall in W 15 also. Generally speaking, the variation rules of the vertical bending moments obtained by the three methods are basically consistent, and the SMR are just slightly larger than the TCR and NSR and closer to the TCR, which more precisely illustrates that the proposed CCSTCM and the numerical calculation model established are correct and reliable.

8. Conclusions

In view of the shortcomings of existing calculation methods for circular diaphragm walls, as well as their own structural characteristics and mechanical characteristics, an alternative calculation method was developed with clear concept based on the circular cylindrical shell theory and superposition principle in elasticity. Taking the north anchorage circular foundation pit of G3 Tongling Yangtze River Highway and Railway Bridge as a case study, the proposed CCSTCM in this study was used to calculate and analyze, and its applicability and correctness were also proven. The specific research content is as follows.

(1) Because the circular diaphragm wall of the north anchorage foundation pit was mainly subjected to horizontal loads in the construction process, the mechanical calculation model of the circular diaphragm wall under the axisymmetric normal loads was given according to the mechanical characteristics of the circular diaphragm wall.
(2) The circular diaphragm wall of the north anchorage foundation pit was simplified into a circular cylindrical shell model. The calculation formulas of the internal force and deformation of the circular diaphragm wall under axisymetric normal loads were derived by the circular cylindrical shell theory in elasticity, and the analytical solution and calculation steps based on the elastic superposition principle were provided.
(3) The numerical model of the whole construction process of the north anchorage circular foundation pit was established, and the site monitoring of Section A was carried out.
(4) The proposed CCSTCM and the FENSM were used to calculate the engineering case, and then the radial displacement, circumferential stress and vertical bending moment of the circular diaphragm wall under normal loads were obtained. All the obtained results were summarized regularly, and the numerical calculation model established was proven to be correct and reliable.

(5) The TCR and NSR were compared with the SMR. On the whole, the TCR values were slightly larger than the NSR values, but slightly smaller than and closer to the SMR. Moreover, the curves obtained from the CCSTCM were highly similar to those obtained from the FENSM and site monitoring. All these facts fully prove the rationality and correctness of the CCSTCM proposed.

Author Contributions: Conceptualization, L.W.; methodology, L.W. and G.S.; software, L.W.; formal analysis, L.W.; supervision, L.W.; investigation, L.W. and G.S.; resources, L.W.; validation, G.S.; visualization, L.W.; writing—original draft, L.W.; writing—review and editing L.W. All authors have read and agreed to the published version of the manuscript.

Funding: This research was supported by the Nantong Science and Technology Plan Program (JC22022082) and Postgraduate Research and Practice Innovation Program of Jiangsu Province (KYCX23_0000).

Institutional Review Board Statement: Not applicable.

Informed Consent Statement: Not applicable.

Data Availability Statement: Data can be obtained from the corresponding author upon reasonable.

Conflicts of Interest: The authors declare no conflict of interest.

References

1. Tan, Y.; Wang, D.L. Characteristics of a large-scale deep foundation pit excavated by the central-island technique in Shanghai soft clay. I: Bottom-up construction of the central cylindrical shaft. *J. Geotech. Geoenviron. Eng.* **2013**, *139*, 1875–1893. [CrossRef]
2. Ling, X.; Wang, R.H. Seepage analysis and construction practice of anchorage circular foundation excavation in long-span suspension bridge. *Appl. Mech. Mater.* **2011**, *90–93*, 128–132. [CrossRef]
3. Seitz, J.M. Diaphragm walls for deep shafts for the anchorage of a suspension bridge in Africa. In Proceedings of the Grouting 2017, Honolulu, Hawaii, 9–12 July 2017; Grouting 2017 GSP 289; pp. 491–501.
4. Yong, Y.; Wu, Y.G.; Xu, G.P.; Gan, Y. Anchorage blocks of the Second Humen Bridge. In *High Tech Concrete: Where Technology and Engineering Meet, Proceedings of the 2017 fib Symposium, Maastricht, The Netherlands, 12–14 June 2017*; Springer International Publishing: Berlin/Heidelberg, Germany, 2018; pp. 2654–2659.
5. Gao, X.H.; Tian, W.P.; Li, J.C.; Qi, H.L.; Li, S.Y.; Zhang, Z.P. Research on the stress and deformation characteristics of circular foundation pit during excavation in sand soil. *Adv. Mater. Sci. Eng.* **2023**, *2023*, 3008695. [CrossRef]
6. *JTG 3363-2019*; Specifications for Design of Foundation of Highway Bridges and Culverts. Standards Press of China: Beijing, China, 2019. (In Chinese)
7. Tan, Y.; Wang, D.L. Structural behaviors of large underground earth-retaining systems in Shanghai. I: Unpropped circular diaphragm wall. *J. Perform. Constr. Facil.* **2015**, *29*, 04014058. [CrossRef]
8. Peck, R.B. Deep excavation and tunneling in soft ground. In Proceedings of the 7th International Conference of Soil Mechanics and Foundation Engineering, ISSMGE, Mexico City, Mexio, 29 August 1969; pp. 225–281.
9. Mana, A.I.; Clough, G.W. Prediction of movements for braced cuts in clay. *J. Geotech. Eng. Div.* **1981**, *107*, 759–777. [CrossRef]
10. Clough, G.W.; O'Rourke, T.D. Construction induced movements of in-situ walls. In *Geotechnical Special Publication: Design and Performance of Earth Retaining Structures (GSP 25)*; ASCE: Reston, VA, USA, 1990; pp. 439–470.
11. Ou, C.Y.; Hsieh, P.G.; Chiou, D.C. Characteristics of ground surface settlement during excavation. *Can. Geotech. J.* **1993**, *30*, 758–767. [CrossRef]
12. Hsieh, P.G.; Ou, C.Y. Shape of ground surface settlement profiles caused by excavation. *Can. Geotech. J.* **1998**, *35*, 1004–1017. [CrossRef]
13. Long, M. Database for retaining wall and ground movements due to deep excavations. *J. Geotech. Geoenviron. Eng.* **2001**, *127*, 203–224. [CrossRef]
14. Moormann, C. Analysis of wall and ground movements due to deep excavation in soft soils based on a new worldwide database. *Soils Found.* **2004**, *44*, 87–98. [CrossRef]
15. Kung, G.T.C.; Juang, C.H.; Hsiao, E.C.L.; Hashash, Y.M.A. Simplified model for wall deflection and ground-surface settlement caused by braced excavation in clays. *J. Geotech. Geoenviron. Eng.* **2007**, *133*, 731–747. [CrossRef]
16. Liu, Y.D.; Hu, W.; Huang, D.X. The response of somatotype characteristics of circular underground diaphragm wall structure. *Adv. Mater. Res.* **2014**, *1065–1069*, 1290–1295. [CrossRef]
17. Cui, J.F.; Hu, J.H.; He, Y.B. Force analysis of circular underground diaphragm wall based on Ritz Method. *China J. Highw. Transp.* **2017**, *30*, 48–55. (In Chinese)
18. Cai, F.; Ugai, K.; Hagiwara, T. Base stability of circular excavations in soft clay. *J. Geotech. Geoenviron. Eng.* **2002**, *128*, 702–706. [CrossRef]

19. Arai, Y.; Kusakabe, O.; Murata, O.; Konishi, S. A numerical study on ground displacement and stress during and after the installation of deep circular diaphragm walls and soil excavation. *Comput. Geotech.* **2008**, *35*, 791–807. [CrossRef]
20. Borges, J.L.; Guerra, G.T. Cylindrical excavations in clayey soils retained by jet grout walls: Numerical analysis and parametric study considering the influence of consolidation. *Comput. Geotech.* **2014**, *55*, 42–56. [CrossRef]
21. Wu, G.J.; Chen, W.Z.; Bian, H.B.; Yuan, J.Q. Structure optimisation of a diaphragm wall with special modelling methods in a large-scale circular ventilating shaft considering shield crossing. *Tunn. Undergr. Space Technol.* **2017**, *65*, 35–41. [CrossRef]
22. Kumagai, T.; Ariizumi, K.; Kashiwagi, A. Behaviour and analysis of a large-scale cylindrical earth retaining structure. *Soils Found.* **1999**, *39*, 13–26. [CrossRef] [PubMed]
23. Parashar, S.; Mitchell, R.; Hee, M.W.; Sanmugnathan, D.; Nicholson, G. Performance monitoring of deep shafts at Changi WRP project. In Proceedings of the 7th FMGM 2007: Field Measurements in Geomechanics, Singapore, 24–27 September 2007; pp. 1–12.
24. Jia, J.; Zhai, J.Q.; Li, M.G.; Zhang, L.L.; Xie, X.L. Performance of large-diameter circular diaphragm walls in a deep excavation: Case study of Shanghai Tower. *J. Aerosp. Eng.* **2019**, *32*, 04019078. [CrossRef]
25. Cabarkapa, Z.; Milligan, G.W.E.; Menkiti, C.O.; Murphy, J.; Potts, D.M. Design and performance of a large diameter shaft in Dublin boulder clay. In Proceedings of the International Conference on Foundations: Innovations, Observations, Design and Practice, Dundee, Scotland, 2–5 September 2003; Thomas Telford Publishing: London, UK, 2003; pp. 175–185.
26. Schwamb, T. Performance Monitoring and Numerical Modelling of a Deep Circular Excavation. Ph.D. Thesis, Department of Engineering, University of Cambridge, Cambridge, UK, 2014.
27. Schwamb, T.; Soga, K. Numerical modelling of a deep circular excavation at Abbey Mills in London. *Géotechnique* **2015**, *65*, 604–619. [CrossRef]
28. Shi, H.; Jia, Z.L.; Wang, T.; Cheng, Z.Q.; Zhang, D.; Bai, M.Z.; Yu, K. Deformation characteristics and optimization design for large-scale deep and circular foundation pit partitioned excavation in a complex environment. *Buildings* **2022**, *12*, 1292. [CrossRef]
29. Xu, Z.L. *Elasticity (Second Volume)*; Higher Education Press: Beijing, China, 2016. (In Chinese)
30. Timoshenko, S.; Woinowsky-krieger, S. *Plate and Shell Theory. Translation Team for "Plate and Shell Theory" Translating*; Science Press: Beijing, China, 1977. (In Chinese)
31. Li, Q.Y.; Wang, N.C.; Yi, D.Y. *Numerical Analysis*, 5th ed.; Huazhong University of Science & Technology Press: Wuhan, China, 2018. (In Chinese)

Disclaimer/Publisher's Note: The statements, opinions and data contained in all publications are solely those of the individual author(s) and contributor(s) and not of MDPI and/or the editor(s). MDPI and/or the editor(s) disclaim responsibility for any injury to people or property resulting from any ideas, methods, instructions or products referred to in the content.